Journal of Energy Storage 106 (2025) 114842

Contents lists available at ScienceDirect

Journal of Energy Storage

journal homepage: www.elsevier.com/locate/est

Research papers

# The power trio: CoS-$CoFe_2O_4$-rGO ternary composite to enhance energy density of all-solid-state asymmetric supercapacitors

S.R. Shingte [a], A.M. Patil [b], Sibylle Gemming [c,d], D.R.T. Zahn [c,d], T.D. Dongale [e], Seong Chan Jun [b,*], G. Salvan [c,d,**], P.B. Patil [a,*]

[a] Department of Physics, The New College, Shivaji University, Kolhapur, Maharashtra 416012, India
[b] Department of Mechanical Engineering, Yonsei University 50 Yonsei-ro, Sinchon-dong, Seodaemun-gu, Seoul, South Korea
[c] Institute of Physics, Chemnitz University of Technology, D-09107 Chemnitz, Germany
[d] Center of Materials, Architectures and Integration of Nanomembranes, Chemnitz University of Technology, 09107 Chemnitz, Germany
[e] School of Nanoscience and Technology, Shivaji University, Kolhapur, Maharashtra 416012, India

ARTICLE INFO

*Keywords:*
Supercapacitor
Asymmetric supercapacitor
Pseudocapacitance
Electric double layer capacitance
Energy density

ABSTRACT

This study addresses a critical challenge in supercapacitors by boosting their energy density without compromising the power density. For this, cobalt sulfide-cobalt ferrite-reduced graphene oxide (CS-CFO-rGO) nanocomposite was prepared using the hydrothermal method and employed as an electrode for supercapacitors. Detailed analysis of X-ray photoelectron spectroscopy and ab initio density functional theory confirmed the presence of cobalt ferrite nanocrystals with both normal and inverse occupation types, which is the most suitable phase of CFO for the supercapacitor applications. The CS-CFO-rGO composite synergistically combined the large specific surface area offered by the flower-like structure of CS, significant conductivity of rGO, and abundant electroactive sites of both the CFO and CS which led to improved overall supercapacitive performance. The ternary composite exhibited a superior specific capacitance of 1381 F $g^{-1}$ at 0.5 A $g^{-1}$. An asymmetric supercapacitor (ASC) device was fabricated which achieved 55.25 Wh $kg^{-1}$ energy density and 375 W $Kg^{-1}$ power density with notable stability. The practical applicability of the ASC device was demonstrated by powering LEDs.

## 1. Introduction

The evolution of affordable and effective energy storage devices is highly desired due to the increasing use of electric automobiles, portable and wearable electronics, etc. For this, electrochemical supercapacitors (SCs) are appealing due to their exceptional power density, affordable cost, adjustable capacities, and outstanding reversibility [1]. However, compared to batteries, SCs have relatively low energy density (E.D.) which may limit the scope of their potential future applications. Consequently, while maintaining a high-power density (P.D.) increasing the E.D. of SCs is crucial. The E.D. depends on both the capacitance and operating potential via ($E.D. = \frac{1}{2}CV^2$) [2]. Hence, the E.D. can be improved by increasing the specific capacitance of electrode materials and extending the cell potential [3].

SCs can be classified into two groups depending on their energy storage principle: pseudocapacitors (PCs) and electrical double-layer capacitors (EDLCs) [4,5]. PCs store energy by redox reactions, while EDLCs store energy by accumulating charge. Pseudocapacitive transition metal sulfides and oxides have gained widespread attention for SCs owing to their substantial theoretical capacity and multiple oxidation states allowing for efficient redox charge transfer with suitable electroactive sites, chemical stability, thermal stability [6,7], and endurance of valence state switching in the memristive context [8]. A class of transition metal sulfides, such as MoS [9], CoS [10], NiS [11], MnS [12], and FeS [13] have been tested for SC applications. Cobalt sulfide (CS) is considered a highly promising material as an electrode because of the availability of various crystalline phases such as $CoS_x$, CoS, $CoS_2$, $Co_3S_4$, etc., and different metal valence states [14]. CoS offers good theoretical capacitance, but its intrinsic conductivity is relatively low. Also, CoS can suffer from volume changes during charge and discharge cycles, leading to electrode degradation and decreasing capacitance over time [15]. To achieve high capacitance, good rate capability, and excellent cycling life in a supercapacitor electrode, the material needs both high theoretical capacitance and excellent mechanical and chemical stability. Among

* Corresponding authors.
** Correspondence to: P. B. Patil, Department of Physics, The New College, Shivaji University, Kolhapur, Maharashtra 416012, India.
*E-mail addresses:* scj@yonsei.ac.kr (S.C. Jun), salvan@physik.tu-chemnitz.de (G. Salvan), prashantphy@gmail.com (P.B. Patil).

https://doi.org/10.1016/j.est.2024.114842
Received 18 July 2024; Received in revised form 10 November 2024; Accepted 28 November 2024
Available online 30 November 2024

different transition metal oxides, especially those belonging to the ferric series ($MFe_2O_4$, where M = $Co^{2+}$, $Ni^{2+}$, $Zn^{2+}$), $CoFe_2O_4$ is the most suitable for it because of its high specific capacitance and chemical stability [16]. However, in the case of both CoS and $CoFe_2O_4$, the slow movement of ions and volume changes during the redox process lead to low conductivity, poor cycle life, and unstable structures [17]. Recent research has shown that the combination with graphene or its derivatives, such as reduced graphene oxide (rGO), can enhance and expand the functionalities of metal sulfides and oxides [18,19]. These composites have an increased electrochemically active surface area and high electrical conductivity [20,21]. Furthermore, the composites can effectively prevent sulfide/metal oxide agglomeration and excessive volume expansion [21]. A study by Sankar et al., [22], reported a specific capacitance of 123.2 F $g^{-1}$ for an rGO-$CoFe_2O_4$ composite at a current density of 5 mA $cm^{-2}$. This is significantly higher than the 18.7 F $g^{-1}$ measured for pristine $CoFe_2O_4$. Various binary and ternary composites such as $NiFe_2O_4/MoS_2$ [23], $MnFe_2O_4/MoS_2$ [24], $MoS_2$-$Fe_3O_4$-rGO [25], etc. have been reported recently for SC application with improved electrochemical performance compared to individual components. The redox-based CoS and $CoFe_2O_4$ with high theoretical capacity and EDLC-based rGO with high electrical conductivity can complement each other through synergistic effects and can enhance the overall supercapacitive performance of composite material. The E.D. of a supercapacitor can further be increased by constructing an all-solid-state asymmetric supercapacitor (ASC) device that combines two distinct electrodes to extend the working potential window [26–28]. Recently, Gao et al. fabricated a $CoFe_2O_4$//activated carbon device which delivered an E.D. of ~22.85 Wh $kg^{-1}$ at a power density of 900 W $kg^{-1}$ [29]. Li et al. assembled an asymmetric supercapacitor $NiCo_2S_4$// AC which achieved a maximum E.D. of 41.4 Wh $kg^{-1}$ and a P.D. up to 414 W $kg^{-1}$ [30]. Chand et al. assembled an asymmetric supercapacitor device with activated carbon as an anode and Zeolitic Imidazolate Framework-8 as a cathode which achieved a significant power density of 20,000 W $Kg^{-1}$ for an energy density of 38.89 Wh $kg^{-1}$ [31].

Herein, we report a hydrothermally synthesized ternary composite of cobalt sulfide-cobalt ferrite-reduced graphene oxide (CS-CFO-rGO) which delivered superior electrochemical performance compared to CS and CFO-rGO. The Density Functional Theory (DFT) simulations are incorporated to determine the structures, the phase stability, the chemical shifts, and the resulting formal oxidation states of the Fe and Co semi-core states that dramatically influence the supercapacitive performance. The ASC device was fabricated with a CS-CFO-rGO positive electrode and an activated carbon negative electrode. CS-CFO-rGO//AC device demonstrated 164 F $g^{-1}$ specific capacitance with 55.25 Wh $Kg^{-1}$ E.D. at 375 W $Kg^{-1}$ P.D. with 43 % capacitance retention after 10,000 cycles. Furthermore, ASC devices were used to power red and green LEDs as an applicability test.

## 2. Experimental section

Materials, reagents, and characterization techniques section are provided in the supporting information (S.I.).

### 2.1. Synthesis of electrode materials

#### 2.1.1. Synthesis of cobalt sulfide (CS) nanostructure

The cobalt sulfide nanostructure was synthesized by solvothermal approach as reported previously [32]. Briefly, cobalt chloride hexahydrate (0.2 M) and thiourea (1.2 M) were dissolved in double distilled water (DDW) (20 ml) using magnetic stirring for 30 min. The mixture was then sealed in a Teflon-coated autoclave and heated at 180 °C for 24 h. The obtained product was repeatedly rinsed with ethanol and DDW. It was subsequently air-dried at 60 °C.

#### 2.1.2. Synthesis of cobalt ferrite-reduced graphene oxide (CFO-rGO) nanocomposite

To synthesize the CFO-rGO nanocomposite, the graphene oxide (GO) was initially produced through a modified Hummers' method, using natural graphite flakes as the starting material [33]. The CFO-rGO nanocomposite was synthesized as follows: 37.5 mg GO was dispersed into 15 ml DDW. In the GO dispersion, 150 mg iron (II) nitrate nonahydrate, 46.8 mg cobalt (II) nitrate hexahydrate, and 46.8 mg cetyltrimethylammonium bromide (CTAB) were added by stirring for 2 h. The pH of the resulting mixture was carefully brought to 9 by the controlled addition of 25 % ammonia solution with vigorous stirring. The obtained uniform solution was loaded into a Teflon autoclave and was maintained at 180 °C for 15 h. The mechanism involved in the formation of the CFO-rGO composite is explained in the supplementary information (SI). After synthesis, the CFO-rGO powder was washed thoroughly with DDW and ethanol. Finally, the powder was dried at 80 °C for 2 h.

#### 2.1.3. Synthesis of cobalt sulfide-cobalt ferrite-reduced graphene oxide (CS-CFO- rGO) ternary nanocomposite

The CS-CFO-rGO ternary nanocomposite was synthesized by a similar procedure that was used to prepare CFO- rGO (see section 2.1.2) with an addition of CS nanostructure in the reaction mixture. In brief, 37.5 mg CS and GO in a 1:1 ratio were dispersed in 15 ml DDW. Subsequently, 150 mg iron (II) nitrate nonahydrate, 46.8 mg cobalt (II) nitrate hexahydrate, and 46.8 mg CTAB were introduced into the aforementioned dispersion. The solution's pH was brought to 9 by adjusting it with a 25 % ammonia solution. The prepared reaction solution was then autoclaved at 180 °C for 15 h. The final ternary composite was obtained by washing the collected precipitate with ethanol and DDW and dried at 80 °C for 2 h. The flow chart of step-by-step procedures involved in the synthesis of the CS-CFO-rGO hybrid nanocomposite is shown in Fig. S1 of the S.I.

### 2.2. Electrochemical measurements

The supercapacitive behaviour of the synthesized CS, CFO-rGO, and CS-CFO-rGO was first evaluated with a three-electrode configuration using the Metrohm Autolab PGSTAT204 electrochemical workstation. A platinum (Pt) wire served as the auxiliary electrode and an Ag/AgCl as a reference electrode. The working electrode was constructed as follows: A homogeneous slurry of active materials (CS or CFO-rGO or CS-CFO-rGO), activated carbon, and polyvinylidene fluoride (PVDF) with a mass ratio of 8:1:1 was prepared using N-Methylpyrrolidone solvent. The slurry was applied via brush coating onto porous nickel foam (with the exposed area of 1 cm × 1 cm) with 3–5 mg mass loading. The coated film was then dried at 60 °C for 12 h to eliminate all traces of solvent. Finally, the coated Ni foam was subjected to a pressure of 10 tons $m^{-2}$ before using as a working electrode. The aqueous solution of 2 M KOH was used as an electrolyte. Electrochemical techniques such as cyclic voltammetry (CV), galvanostatic charge-discharge (GCD), and electrochemical impedance spectroscopy (EIS) were used.

Asymmetric supercapacitors (ASC) were fabricated by using the CS-CFO-rGO working electrode described above as a positive electrode paired with a negative electrode made of activated carbon. A negative electrode was prepared using a mixture of activated carbon and PVDF with a mass ratio of 9:1. The PVA-KOH (Polyvinyl alcohol- Potassium hydroxide) gel was used as an electrolyte [34]. To prepare PVA/KOH gel electrolyte, 1 g PVA was dissolved in 5 ml DDW and heated for 5 h at 80 °C with continuous stirring. This was then mixed with 5 ml KOH solution (1 M) and stirred until a uniform gel was formed. All-solid-state ASC device was constructed by placing a Whatman paper wetted in gel electrolyte between CS-CFO-rGO and activated carbon electrodes.

## 3. Results and discussion

### 3.1. Physicochemical characterizations

The phase formation and crystal structure of the CS, CFO-rGO, and CS-CFO-rGO nanocomposite samples were studied by X-ray diffraction (XRD), and corresponding patterns along with the standard diffraction data are depicted in Fig. 1A. The XRD pattern CS (a), shows the peaks at 2θ values of 30.72°, 35.45°, 46.85°, 54.80°, and 74.92° indicating cubic CoS phase (JCPDS 03–065-3418). In addition to these peaks, the peaks at 17.24° (200), 26.31° (220), and 32.52° (222) indicate the existence of a minor phase of cubic $Co_9S_8$ (JCPDS 00–019-0364). The presence of a mixed phase in cobalt sulfide nanoparticles can be explained by the intricate composition of cobalt chalcogenides and the strong affinity of cobalt ions to oxygen [35]. In the XRD pattern of CFO-rGO (b), the characteristic peaks at 2θ values of 18.49°, 30.23°, 35.61°, 43.38°, 53.72°, 57.17°, 62.81°, and 74.29°. These peaks can be ascribed to (111), (220), (311), (400), (422), (511), (440), and (533) reflections in a cubic $CoFe_2O_4$ phase with Fd-3 m space group symmetry, which are consistent with the JCPDS. 00–022-1086. Furthermore, the weak diffraction peak at 23.54° is a representation of the (002) lattice planes of the rGO nanosheets [36,37]. The crystallite size (D) of the CFO NPs estimated using the Debye-Scherrer formula from the most prominent (311) peak and it was found to be ~10 nm [38]. In the XRD pattern for the nanocomposite CS-CFO-rGO (c), the peaks at 30.84°, 46.92°, 54.78°, and 74.88° corresponding to the hexagonal CoS phase are present. Interestingly, peaks corresponding to the $Co_9S_8$ are not observed. This could be due to the phase transformation of $Co_9S_8$ to the pure phase of CoS or the selective dissolution of $Co_9S_8$ leaving behind only the pure phase of CoS during the hydrothermal process. Furthermore, crystal planes associated with 2θ values 18.14°, 30.1°, 35.42°, 43.26°, 57°, and 62.72° of $CoFe_2O_4$ along with (002) planes of rGO are observed, indicating the presence of all three phases of CoS, CFO, and rGO in the ternary composite. A shift in 2θ values towards lower values can be seen which is ascribed to the changes in lattice parameters due to interactions between the components of the nanocomposite [39]. The crystallinity of rGO in the ternary composite appears to be low and the diffraction peaks are broad, which can be attributed to its weak scattering power in the hybrid nanocomposite.

To understand the microstructure and chemical bonding of the materials, Raman analysis is performed and Raman spectra of CS, CFO-rGO, and CS-CFO-rGO are unveiled in Fig. 1B. In the spectrum of CS (Fig. 1B (a)), a peak around 464 $cm^{-1}$ represents the $E_g$ stretching mode resulting from the vibrations between the Co and S atoms [39]. The peaks at 509 $cm^{-1}$ and ~ 659 $cm^{-1}$ are due to the $F^1_{2g}$ and $A_{1g}$ vibrational modes of the Co—S bond respectively [40]. An observed peak at 188 $cm^{-1}$ suggests the presence of the $Co_9S_8$ phase [41]. The Raman spectrum of CFO-rGO shown in Fig. 1B (b) exhibits Raman-active modes $T_{2g}$, $E_g$, and $A_{1g}$ located at 452 $cm^{-1}$, 295 $cm^{-1}$, and 667 $cm^{-1}$ respectively. The $T_{2g}$ modes in spinel $CoFe_2O_4$ refer to the vibrational movement of the lattice or oxygen atoms located in the octahedral sites. In octahedral geometries, the $E_g$ vibrational mode corresponds to the symmetric and antisymmetric bending of oxygen ions in the M-O bond [42]. The $A_{1g}$ mode represents the vibration originating from the oxygen atoms around the tetrahedral sites in spinel $CoFe_2O_4$ [43]. The G band (1597 $cm^{-1}$) represents the scattering of the $E_{2g}$ mode observed in $sp^2$ C domains in rGO. Further, the D band (1344 $cm^{-1}$) corresponds to the edge plane and disordered structure of the aromatic rings, thus suggesting the presence of rGO nanosheets. It seems that the CFO and rGO are not undergoing a chemical reaction, but rather they are exhibiting interface interaction, which results in the observation of a D band peak [44]. The Raman spectrum of the nanocomposite CS-CFO-rGO, shown in Fig. 1B (c), also reveals the presence of rGO nanosheets through the two distinct D and G bands at 1352 $cm^{-1}$ and 1592 $cm^{-1}$. The shift in the wavenumber of D and G bands in CS-CFO-rGO compared to CFO-rGO nanosheets suggests the interaction between the CS and CFO-rGO moieties [45]. Additionally, it has the various Raman peaks associated with CS and $CoFe_2O_4$. The $A_{1g}$ (682 $cm^{-1}$) and $E_g$ (343 $cm^{-1}$) peaks can be accredited to the $CoFe_2O_4$ spinel crystal. Meanwhile, the band at 466 $cm^{-1}$ is a result of the Co—S vibration and represents the $E_g$ stretching mode. Interestingly,

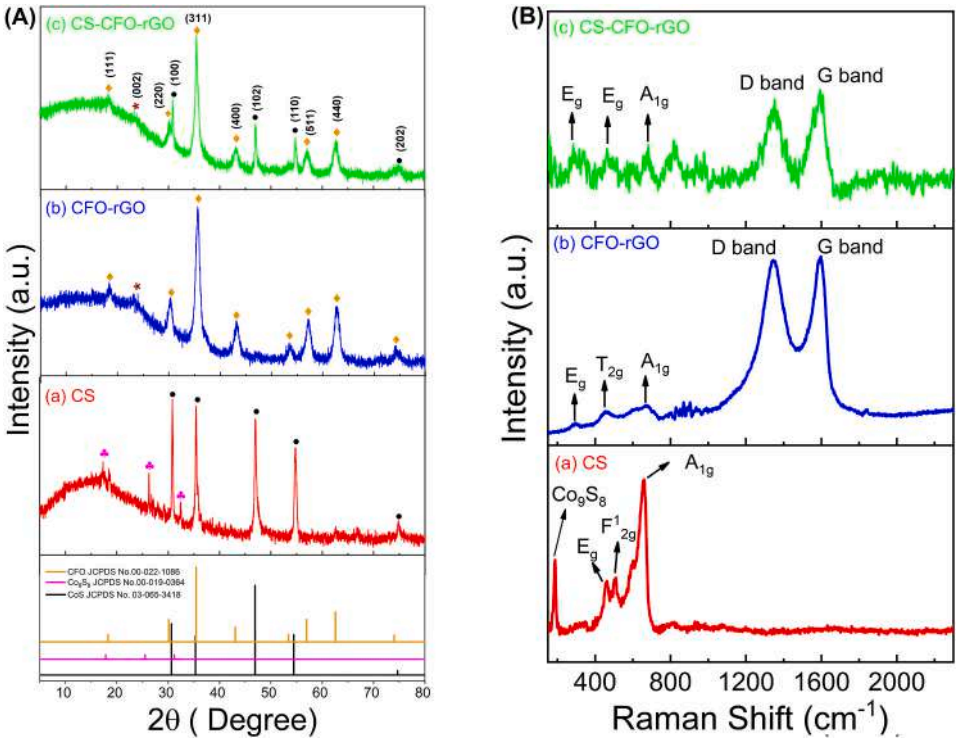


**Fig. 1.** (A) XRD patterns of the CS (a), CFO-rGO (b), and CS-CFO-rGO (c). The lower panel shows the standard diffraction data of CoS (JCPDS. 03–065-3418), $Co_9S_8$ (JCPDS. 00–019-0364), and $CoFe_2O_4$ (JCPDS. 00–022-1086). (B) Raman spectra of CS (a), CFO-rGO (b), and CS-CFO-rGO (c).

the absence of the 2D-band of rGO in both CFO-rGO and CS-CFO-rGO samples is likely due to the network structure of rGO instead of a single layer of graphene. Furthermore, the multilayer nature of rGO is also confirmed by the $I_D/I_G$ ratio of CFO-rGO and CS-CFO-rGO which is 1.11 and 0.91, respectively. This confirms the successful integration of rGO with CoS and CFO nanostructures and is corroborated with the XRD results.

Low- and high-resolution scanning electron microscope (SEM) images were recorded to investigate the morphological features of nanostructured CS, CFO-rGO, and CS-CFO-rGO (Fig. 2). The SEM image of CS in Fig. 2 (a & b) displayed a flower-like hierarchical microsphere made up of nanoplates. The numerous interleaving nanoplates (each around 150 nm thick) are assembled to form flower-like structures of average 9 μm size. This hierarchical porous structure with three dimensions offers a significant increase in the surface area thereby facilitating efficient interaction between the CS electrode and electrolyte ions [32]. The SEM image of CFO-rGO depicted in Fig. 2 (c & d) reveals the random distribution of aggregated $CoFe_2O_4$ nanoparticles on rGO sheets. Similarly, in the image of the CS-CFO-rGO ternary nanohybrid composite shown in Fig. 2 (e & f), CoS and CoFe oxide moieties with crumpled silk-like and interconnected rGO nanosheets can be seen. The elemental mapping of CoS, CFO-rGO, and CS-CFO-rGO from SEM is provided in Fig. S2. In the ternary composite, the NPs make up a large portion of the layered structure, appearing to be situated adjacent to each other on the rGO layer surface and looking like aggregation. Despite this, the size of each nanoparticle remains relatively small, measuring around 12 nm in diameter. The randomly distributed nanoparticles on rGO sheets can increase the overall surface area of the electrode, potentially creating an abundance of active sites for storing electrical charges and thus higher capacitance. Further, the rGO sheets act as a support to the NPs, elevating the electrical conductivity of the electrode composite. On the other side, the decoration of NPs on rGO sheets can improve the stability of the SCs, as the nanoparticles can act as a protective layer for the rGO sheets and prevent them from degradation [46].

A detailed microstructural and compositional analysis of CoS, CFO-rGO, and CS-CFO-rGO was performed using transmission electron microscopy (TEM) (Fig. 3). Low and high-power TEM micrographs of the CoS sample shown in Fig. 3A (a & b). These flakes self-assembled together to form a flower-like hierarchical structure of CoS microspheres as observed in the SEM image (Fig. 2a). Fig. 3A(c) reveals a well-defined ring pattern in the selected area electron diffraction (SAED) analysis, consistent with the characteristic diffracting planes (100), (102), (110), and (202) of a cubic CoS structure. The composition of all three materials was obtained by EDX measurements and spectra are shown in Fig. S3. The measured atomic percentages of Co and S in CoS are 44.49 and 14.70, respectively, which may be due to the mixed phases of CoS and $Co_9S_8$. The surface composition of CoS was further confirmed by elemental mapping and is shown in Fig. 3A (d), suggesting the uniform distribution of cobalt and sulfur. The TEM images (Fig. 3B (a & b)) show that $CoFe_2O_4$ NPs are decorated on the surface of rGO nanosheets in a dense form. Importantly, no obvious large and aggregated $CoFe_2O_4$ nanoparticles are visible, and no naked rGO sheets or free $CoFe_2O_4$ nanoparticles appear. The size distribution of the CFO NPs was determined by analyzing several TEM images and is shown in Fig. S4(A). The typical size of NPs was determined to be $10.9 \pm 0.2$ nm. The SAED pattern of the CFO-rGO nanocomposite shown in Fig. 3B (c) has rings corresponding to the cubic structure of spinel $CoFe_2O_4$ crystals. Elemental mapping analysis of the CFO-rGO composites was performed to illustrate the spatial distribution of carbon, cobalt, iron, and oxygen in the composite (Fig. 3B (d)). The TEM micrographs of CS-CFO-rGO shown in Fig. 3C (a & b) demonstrated that the wrinkled paper-like rGO sheets are covered by the CoS and CFO NPs. Little agglomerations in CoS and CFO NPs of CS-CFO-rGO were observed which could be possibly due to the magnetic forces that exist between the nanoparticles and high surface area [47]. The presence of rGO sheets may help to prevent NPs from clumping together, ensuring better cyclability [48]. The SAED image of CS-CFO-rGO (Fig. 3C (c)) shows a pattern of regularly spaced diffraction spots, which have been attributed to the (311), (440), and (731) planes of $CoFe_2O_4$ and another set to the (102), (211) planes of CoS. The elemental distribution of CS-CFO-rGO is investigated by EDS mapping as shown in (Fig. 3C (d)) which shows that CS-CFO-rGO is composed of uniformly distributed Fe, Co, O, C, and S. This uniform and dense distribution of the cobalt ferrite NPs enabled by the CoS NPs lead to an increased surface area relative to their volume. This enhanced surface-to-volume ratio facilitates improved charge transfer at the electrode, ultimately resulting in greater capacitance. The average particle diameter was estimated to be around $12 \pm 0.2$ nm, as revealed by the particle size distribution histogram (Fig. S4(B)). A High-resolution TEM image of CS-CFO-rGO and the corresponding inverse Fast-Fourier Transform (FFT) analysis is demonstrated in Fig. S5. The lattice fringe spacing of CFO and CoS were determined to be 2.52 Å and 2.83 Å, indicating the presence of (311) planes of cubic crystal CFO

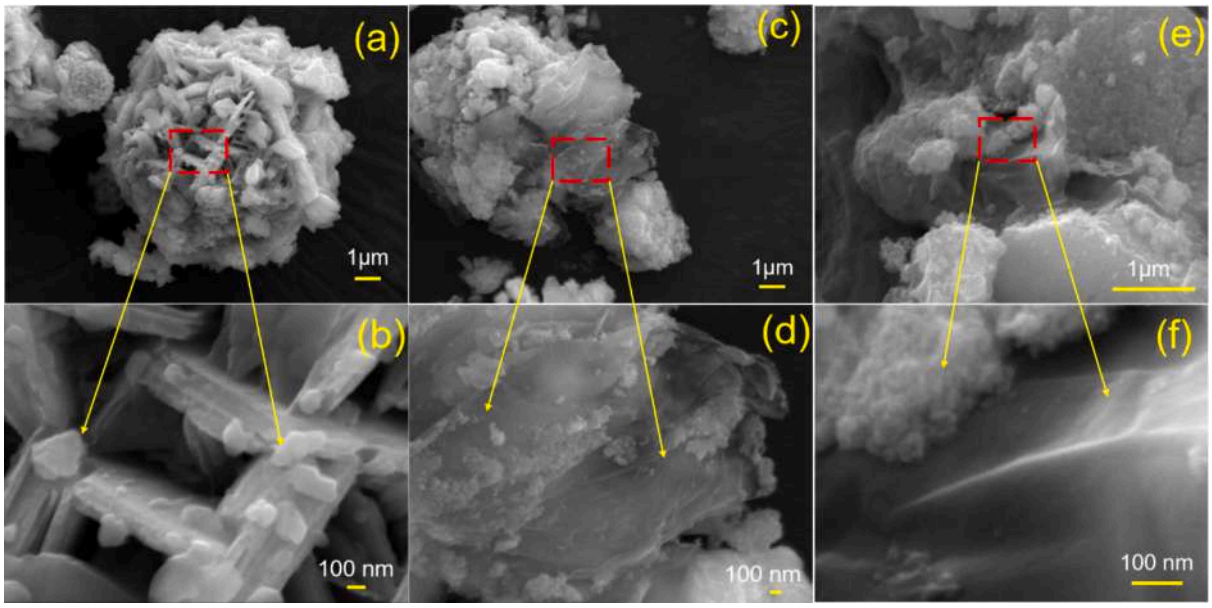


**Fig. 2.** Low- and high-resolution SEM images of CS (a, b), CFO-rGO (c, d), and CS-CFO-rGO (e, f).

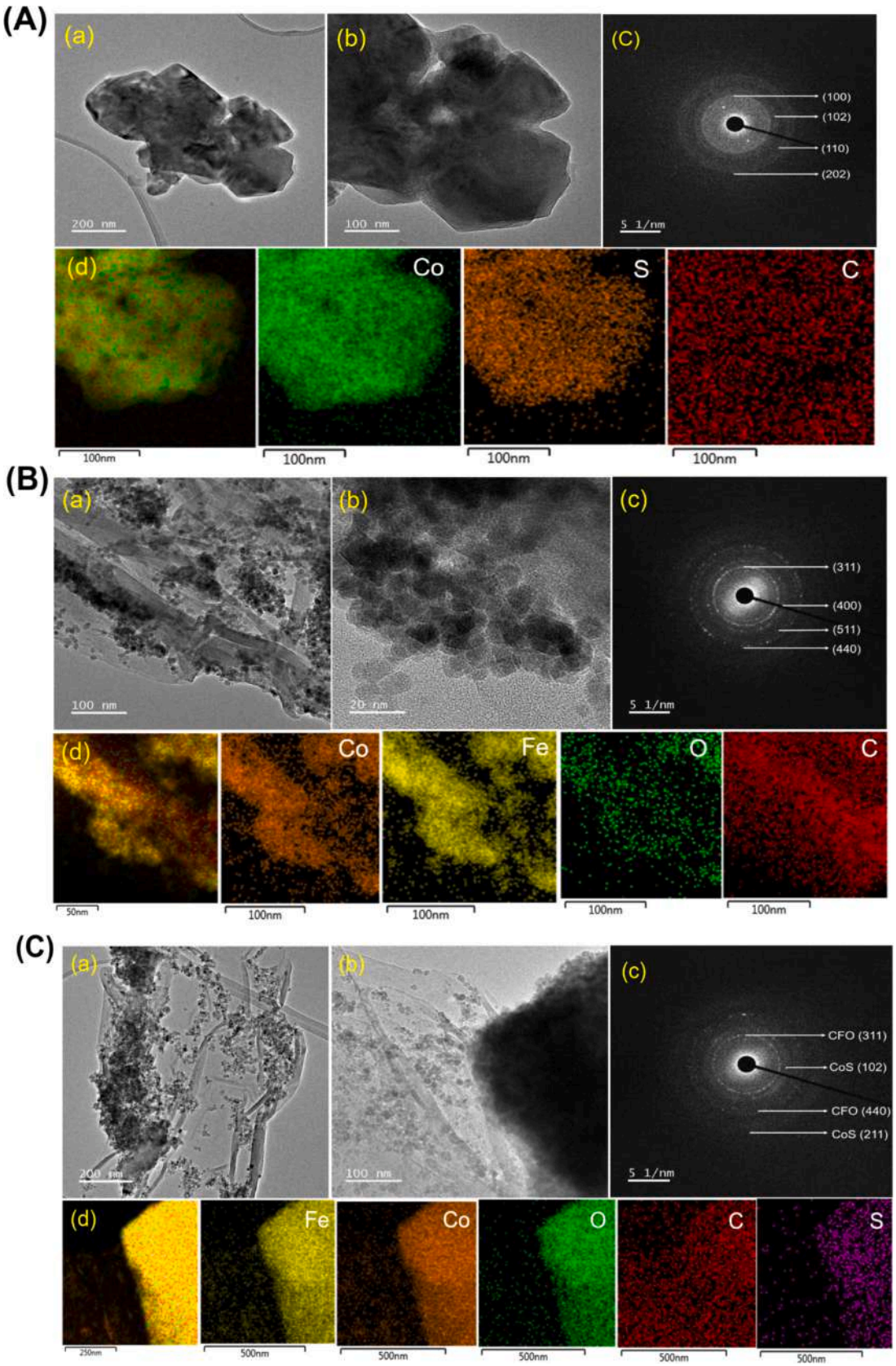


**Fig. 3.** Low and high-power TEM micrographs (a, b), SAED pattern (c), and corresponding elemental mapping (d) of CoS (A), CFO-rGO (B), and CS-CFO-rGO (C).

(JCPDS. No. 00–022-1086) and (100) planes hexagonal crystal of CoS (JCPDS No. 03–065–3418), respectively. Furthermore, the lattice spacing of 3.46 Å corresponding to (002) planes of hexagonal structured rGO was also observed. This confirms the presence of CoS, CFO, and rGO in the ternary composite. The Co chemical potential is set by the presence of the $Co^{2+}$-containing CoS nanocrystals, which not only supports the formation of $CoFe_2O_4$ over $FeCo_2O_4$ but also suppresses the formation of $Co_3O_4$, which occurs as an undesirable side product of irreversible deep discharge of Li-based battery materials and does not have the high capacity of the ternary oxides to store and release electrons [49,50]. In accordance with prior studies a slight energetic preference for the inverse spinel structure of $CoFe_2O_4$ is obtained by first-principles investigations (see S.I.). Thus, the corroboration of theoretical and experimental results in this study supports the presence of cobalt ferrite nanocrystals with both normal and inverse occupation types.

The X-ray photoelectron spectroscopy (XPS) was used to study the chemical structure and valence states of the CS-CFO-rGO nanocomposite and the results are shown in Fig. 4. The survey scan of the nanocomposite, presented in Fig. 4A, reveals the presence of the elements Fe (710.08 eV), Co (779.08 eV), S (165.50 eV), C (283.08 eV), O (530.08 eV), and an Auger signal of OKLL (975.08 eV). The Co 2p spectrum with high resolution (Fig. 4B) revealed two spin-orbit doublets. These doublets at 779.80 eV and 794.88 eV represent the Co $2p_{3/2}$ and Co $2p_{1/2}$ electronic states of the $Co^{2+}$ state. Further, the Co $2p_{3/2}$ peak is deconvoluted into two distinct peaks at 779.34 eV and 780.30 eV consistent with the electronic states $Co^{2+}$ (Oh) and $Co^{2+}$ (Th) in spinel ferrite, respectively. The peaks observed at 785.16 eV and 801.35 eV are satellite peaks of Co $2p_{3/2}$ and Co $2p_{1/2}$, respectively [51]. The S 2p spectrum in Fig. 4C exhibits two spin-orbit peaks with binding energies 161.38 and 167.58 eV [52]. The peak at 161.38 eV is indicative of the presence of $S^{2-}$. On the other hand, the peak at 167.58 eV likely originates from partial oxidation of sulfur in the air which results in the formation of stronger ionic chemical bonds with Co atoms [53]. The Fe 2p spectrum (Fig. 4D) has Fe $2p_{3/2}$ and Fe $2p_{1/2}$ peaks for the $Fe^{3+}$ state at 709.68 eV and 723.7 eV, respectively. Fe $2p_{3/2}$ main peak is accompanied by a satellite peak at 717.45 eV. This satellite peak is further fitted into two signals positioned at 709.48 eV and 712.25 eV, which are due to $Fe^{3+}$ ions at octahedral and tetrahedral lattice sites [54]. Furthermore, the deconvoluted C 1 s spectrum (Fig. 4E) displays peaks are correlated with the C═C ($sp^2$ bonded, 283.52 eV), C—O (oxygenated carbon, 286.27 eV), and C═O (carbonyl, 287.52) groups of rGO [55]. The C—O and C═O linkage suggest that GO was reduced to rGO. In the XPS spectrum of O 1 s (Fig. 4F), the peak at 530.38 eV is related to the Co—O bond in the $CoFe_2O_4$ interfacial bonding structure [44]. The other peak at 528.89 eV corresponds to the metal-oxygen-carbon bond, indicating a covalent bonding between cobalt ferrite NPs and the rGO sheets [56]. This assignment of the Co-, Fe- and O-type spectra is supported by a first-principles analysis of the 3p semi-core states of Co and Fe, and of the 2 s valence states of O (S.I.).

$N_2$ gas adsorption-desorption measurements were employed in conjunction with the Brunauer-Emmett-Teller (BET) method to determine the material's surface area and analyze its pore size. Fig. 5A shows the $N_2$ adsorption-desorption isotherm of CS (a), CFO-rGO (b), and CS-CFO-rGO (c). It depicts that all the plots are of type IV isotherm as classified by the IUPAC [57]. Additionally, the observed H3-type hysteresis loop suggests that the materials have mesoporous characteristics. The surface areas of CS, CFO-rGO, and CS-CFO-rGO are 22.88 $m^2\ g^{-1}$, 75.76 $m^2\ g^{-1}$, and 106.13 $m^2\ g^{-1}$, respectively. The flower-like hierarchical structure of CoS microspheres, the small particle size of $CoFe_2O_4$, and the reduced stacking of rGO nanosheets are reasons for the overall enlargement of the surface area of ternary composite CS-$CoFe_2O_4$-rGO. The pore size distribution of the CS-CFO-rGO is presented in Fig. 5B. For comparison, the pore size distributions of individual CS and CFO-rGO are provided in Fig. S6(A) and S6(B), respectively. The increased surface area and larger pore volume provide room for more active material to be present on the electrode. This configuration not only allows for easier penetration of the electrolyte into the active material but also minimizes resistance. This may lead to the improved overall efficiency of the supercapacitor in terms of electrochemistry [58,59]. Additionally, the presence of mesopores can provide more sites for the storage of charged particles, further increasing the energy storage capacity of the supercapacitor [60]. The key findings of the BET measurements are presented in Table 1.

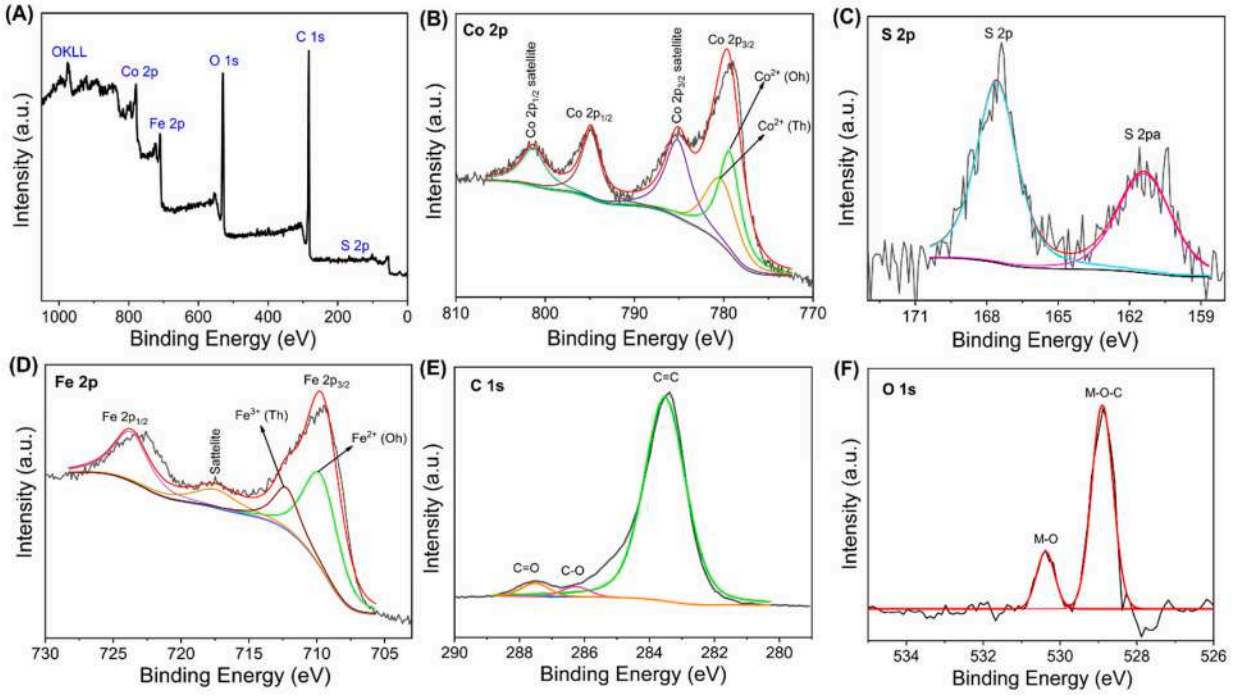


**Fig. 4.** XPS survey spectrum of the CS-CFO-rGO (A). The high-resolution XPS spectrum of Co 2p (B), S 2p (C), Fe 2p (D), C 1 s (E), and O 1 s (F).

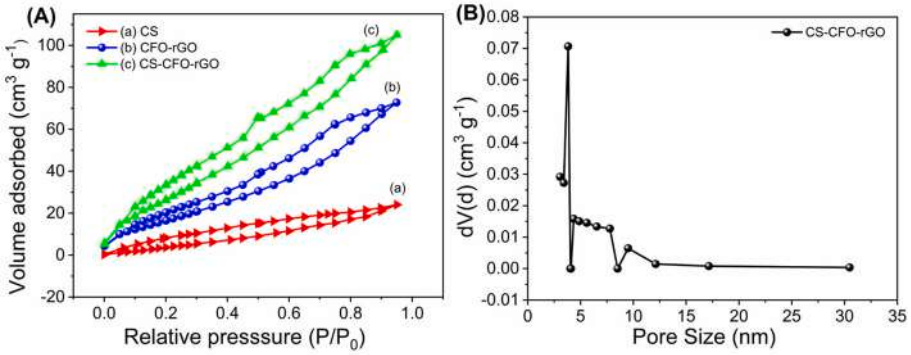


**Fig. 5.** (A) $N_2$ adsorption-desorption isotherm of CS (a), CFO-rGO (b), and CS-CFO-rGO (c). (B) Pore size distribution of CS-CFO-rGO.

**Table 1**
Specific surface area ($S_{BET}$), pore volume ($V_{pores}$), and average pore size ($d_{pores}$) of CS, CFO-rGO, and CS-CFO-rGO samples.

| Samples | $S_{BET}$ ($m^2\ g^{-1}$) | $V_{pores}$ ($cm^3\ g^{-1}$) | $d_{pores}$ (nm) |
|---|---|---|---|
| CS | 22.33 | 0.029 | 4.03 |
| CFO-rGO | 75.76 | 0.106 | 4.044 |
| CS-CFO-rGO | 106.129 | 0.141 | 3.821 |

### 3.2. Electrochemical performance in a three-electrode system

To understand the reduction-oxidation mechanisms of molecular species and ascertain the appropriate operating potential window of the electrode material, CV curves of bare Ni foam, CS, CFO-rGO, and CS-CFO-rGO were recorded at 10 mV $s^{-1}$ (Fig. 6A). The CV profiles show that all three samples have distinctive reduction-oxidation peaks which demonstrate pseudocapacitive behaviour controlled by faradaic processes [61]. Interestingly, the CV shapes of the electrodes display significant diversity, which is explained by the various redox reactions occurring in the active materials. The *CV* curve a, representing the Ni foam substrate, exhibits a quasi-straight line, implying a negligible role of Ni foam in overall capacitance. The well-defined redox peaks in the CV curve of CS (curve b) suggest a reversible faradaic process, indicating efficient electron transfer between the electrode and the analyte [62,63],

$$CoS + OH^- \leftrightarrow CoSOH + e^- \quad (1)$$

$$CoSOH + OH^- \leftrightarrow CoSO + H_2O + e^- \quad (2)$$

Since sulfur belongs to the same chemical family as oxygen it suggests a potential similarity in their behaviour. Interestingly, the electrochemical behaviour of CoS in an alkaline electrolyte exhibits redox peak potentials closely resembling those of $Co(OH)_2$. The observed redox behaviour of CoS in alkaline solutions is mediated by the oxidation and reduction that occur between various cobalt valence states. This observation implies that cobalt in CoS undergoes multiple oxidation states during redox reactions in alkaline environments [64]. The CV curve of CFO-rGO (curve c) shows redox peaks at 0.23 and 0.41 V against Ag/AgCl. Generally, the composite materials made from metal ferrite and reduced graphene oxide (rGO) display both pseudocapacitive properties ($Co/Co^{2+}$ or $Fe/Fe^{2+}$) and EDLC activity [65]. The absence of a rectangular profile implies that charge storage in CFO-rGO primarily

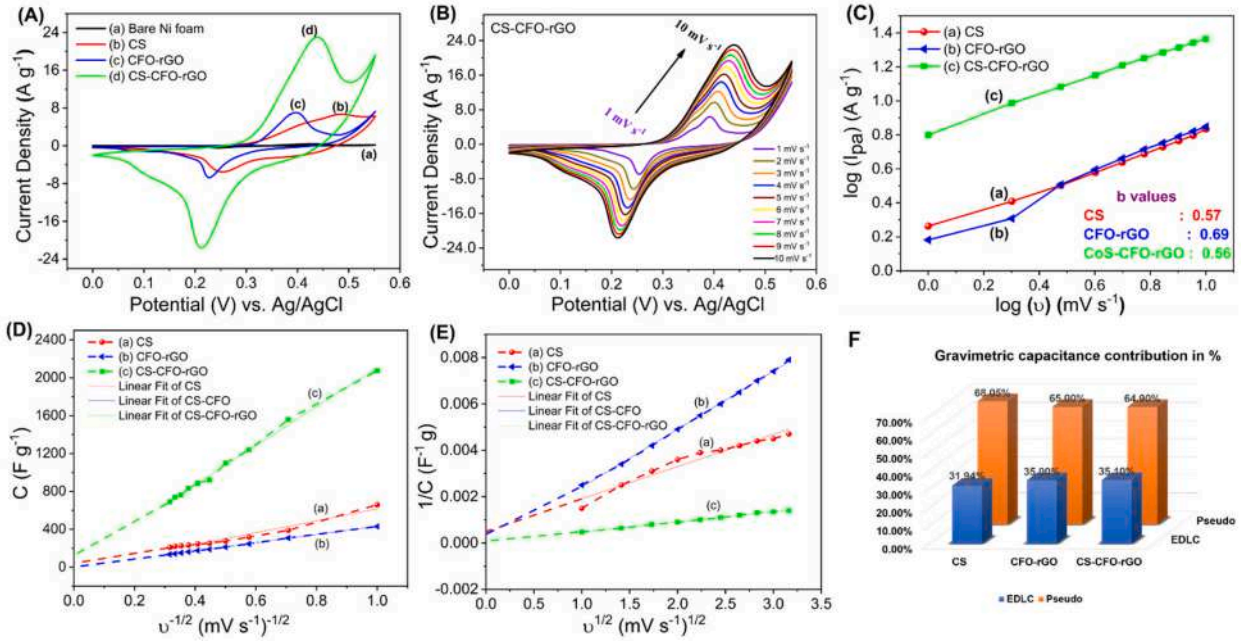


**Fig. 6.** (A) CV curves of bare Ni foam (a), CS (b), CFO-rGO (c), and CS-CFO-rGO (d) at 10 mV $s^{-1}$scan rate. (B) CV profiles of CS-CFO-rGO at 1 to 10 mV $s^{-1}$ scan rate. (C) The plot of log ($I_{pa}$) vs. log (υ) for calculation of b-value. (D) C vs. $υ^{-1/2}$ relation diagram for calculation of gravimetric capacitance contribution of EDLC. (E) 1/C vs. $υ^{1/2}$ relation diagram for calculation of total capacitance of the CS, CFO-rGO, and CS-CFO-rGO. (F) EDLC and pseudocapacitance contribution to the total capacitance of the CS, CFO-rGO, and CS-CFO-rGO estimated from Trasatti analysis.

stems from faradaic reactions involving the transition metals Co and Fe, occurring at the electrolyte-electrode interface [18]. The following equations can illustrate the reaction that occurs between various cobalt and iron oxidation states in the electrolyte [66].

$$CoFe_2O_4 + OH^- + H_2O \leftrightarrow 2\,FeOOH + CoOOH + e^- \quad (3)$$

$$CoOOH + OH^- \leftrightarrow CoO_2 + H_2O + e^- \quad (4)$$

Furthermore, the redox peaks observed in curve d (CS-CFO-rGO) likely correspond to cyclic processes involving reversible reactions between the M-O/M-OOH and M-S/M-S-OH (M = Co or Fe) [23]. In contrast to pure CS and CFO-rGO, the CS-CFO-rGO composite exhibits a substantial rise in current density and an integral area within the CV curve, due to the synergistic actions of three materials in increasing electrochemical reaction activity. To get more insights into the electrochemical behaviour of the CS, CFO-rGO, and CS-CFO-rGO composite, the CVs were recorded using a scan rate of range 1 to 10 mV $s^{-1}$. CVs of CS-CFO-rGO are displayed in Fig. 6B and that of CS and CFO-rGO are shown in Fig. S7(A) and S7(B), respectively. CVs of CS-CFO-rGO at the higher scan rate (10 to 100 mV $s^{-1}$) are shown in Fig. S7(C) to get a more detailed representation of the electrochemical process. The current density of the CS-CFO-rGO composite is increased with increasing scan rate without changing the CV shape. At lower scan rates, the thick double layer forms which slows the migration of fresh electrolyte ions to the surface. On the other hand at higher scan rates, the current density rises due to a thin double layer [67]. Additionally, the observed peak potential shifts with increasing scan rate owing to the limitations in the rate of mass transport within the samples [68]. Such increment in diffusion resistance leads to diffusion-controlled redox reactions and kinetics limited by the charge transfer.

In our electrode materials, both the EDLC and the pseudocapacitive current contribute to capacitive current. The diffusion and intercalation-deintercalation of $K^+$ ions in a KOH electrolyte can be understood by examining the connection between response current (I) and scan rate (υ) [69] as described by

$$I = i_{capacitive} + i_{diffusion} = a\upsilon^b \quad (5)$$

where the variables 'a' and 'b' are modifiable values, and current (I) measured at a stable potential exhibits a power-law dependence on the scan rate (υ). Fig. 6C presents a logarithmic plot of current density ($I_{pa}$) versus scan rate (υ) for the CV profiles of CS, CFO-rGO, and CS-CFO-rGO. The slope, denoted by b, offers valuable information about the rate and mechanism of electrochemical reactions [70]. The b value closer to 1 denotes a capacitive property, whereas the b value closer to 0.5 denotes a diffusive property. Any number between 0.5 and 1 indicates that both faradaic and non-faradaic behaviour is present. The observed values of b for CS, CFO-rGO, and CS-CFO-rGO materials are 0.57, 0.69, and 0.56, respectively, indicating the presence of both types of charge-storage behaviour. The Trasatti analysis was employed to estimate the amount of electrical charge stored by EDLC and pseudocapacitive contribution. The equations used in the Trasatti analysis are [71]:

$$C = k_2\upsilon^{-\frac{1}{2}} + C_{EDL} \quad (6)$$

$$C = k_1\upsilon^{\frac{1}{2}} + \frac{1}{C_T} \quad (7)$$

$$C_{PS} = C_T - C_{EDL} \quad (8)$$

Where, C = gravimetric capacitance, $C_T$ = total specific capacitance, $C_{EDL}$ = electrical double layer capacitance, and $C_{PS}$ = pseudo capacitance, $K_1$ and $K_2$ are the slope and intercept. The $C_{EDL}$ and $C_{PS}$ contributions to total capacitance were calculated using the plots of C vs $\upsilon^{-1/2}$ (Fig. 6D) and the plots of 1/C vs $\upsilon^{1/2}$ (Fig. 6E). Then the amount of charge stored by capacitive and diffusion mechanisms at 10 mV $s^{-1}$ for all three electrode materials is displayed in Fig. 6F.

The electrochemical performance of CS, CFO-rGO, and CS-CFO-rGO materials towards charge storage was evaluated by GCD measurement at 0.5 A $g^{-1}$ current density (Fig. 7A). The discharge curves demonstrate a non-linear behaviour, indicating the dominant pseudocapacitive properties of investigated electrodes at all current densities. This observation is in agreement with the results from CV experiments. A longer discharge time for the electrode correlates to a larger specific capacitance of the material.

The specific capacitances were determined using the formula below:

$$C_{SP} = \frac{I\Delta t}{m\Delta v} \quad (9)$$

Where I denote the discharge current, Δt represents the discharge time, and Δυ symbolizes the potential window. The symbol m refers to the mass of the active material. The nanocomposite CS-CFO-rGO (curve c) exhibits exceptional capacitance due to the combined effect of CS (curve a) and CFO-rGO (curve b) and multiple surface redox reactions, as revealed by CV analysis. Thus, CS-CFO-rGO exhibits a significant capacitance of 1381 F $g^{-1}$. CS has strong redox capabilities, providing active sites for faradaic reactions ensuring efficient access to the electrolyte [25]. While covalent bonding between CFO and rGO ensures fast electron transport [56]. The M-O-C covalent bond also modifies the electronic states of the redox couplings and reduces the electron concentration near the Co/Fe site. Additionally, by preventing the rGO sheets from clumping together and ensuring an even distribution of CFO nanoparticles on the graphene sheets, hybrid material exposes a greater number of active sites and allows smoother transport of oxygen and electrolyte molecules. Further it enhances the available surface area for ion exchange, as confirmed by BET analysis. The GCD of the nanocomposite CS-CFO-rGO (Fig. 7B) was determined at 0.5, 0.75, 1, 2, 3, 4, and 5 A $g^{-1}$ current densities. The results indicated a gradual decrease in the discharge time with increasing current densities. This is attributed to a rise in potential drop and insufficient active electrode material participating in oxidation-reduction reactions at elevated current densities. For better understanding of electrochemical characteristics of the CS, CFO-rGO, and CS-CFO-rGO composite, the GCD behaviour was examined at several current densities (0.5 to 5 A $g^{-1}$). The GCD curves of CS-CFO-rGO are shown in Fig. 7B and that of CS and CFO-rGO are presented in Fig. S8(A) and S8(B), respectively. The electrode demonstrates remarkable performance, maintaining functionality even at exceptionally high current densities. A comparison of the specific capacitance values under different current densities for various nanomaterials investigated is presented in Fig. 7C. CS-CFO-rGO composite acquired a remarkable specific capacitance of 1381 F $g^{-1}$, outperforms both CS nanostructure and CFO-rGO. At 0.5 A $g^{-1}$, CS-CFO-rGO exhibits capacitance of 4.2 times higher that of the CS nanostructure (329 F $g^{-1}$) and 2.7 times that of the CFO-rGO (511 F $g^{-1}$). However, an increase in current density leads to a reduction in specific capacitance. This is mainly because ions are unable to reach the inner part of the electrode before the reaction is completed, thus limiting the reaction to the outer layer of the electrode.

Cyclic stability is a crucial consideration when evaluating the application of supercapacitors. The cyclic stability of the CS-CFO-rGO nanocomposite was evaluated over 10,000 consecutive charge-discharge cycles at 10 A $g^{-1}$ and is displayed in Fig. 7D. After the first few cycles a slight enhancement of the specific capacitance is observed, potentially due to material activation [23]. The nanocomposite retained 78 % of its original capacitance after 2000 cycles and it decreased to 56 % after 10,000 consecutive cycles while achieving 73 % coulombic efficiency. Furthermore, the symmetry of the charge-discharge profiles remained consistent across the examined cycles. The capacitance stability of the CS-CFO-rGO nanocomposite is likely due to the combination of the graphitized structure and the presence of Fe/Co transition metal oxide [66]. Table S1 summarizes the CS-CFO-rGO composite's supercapacitive performance relative to previously reported materials. The

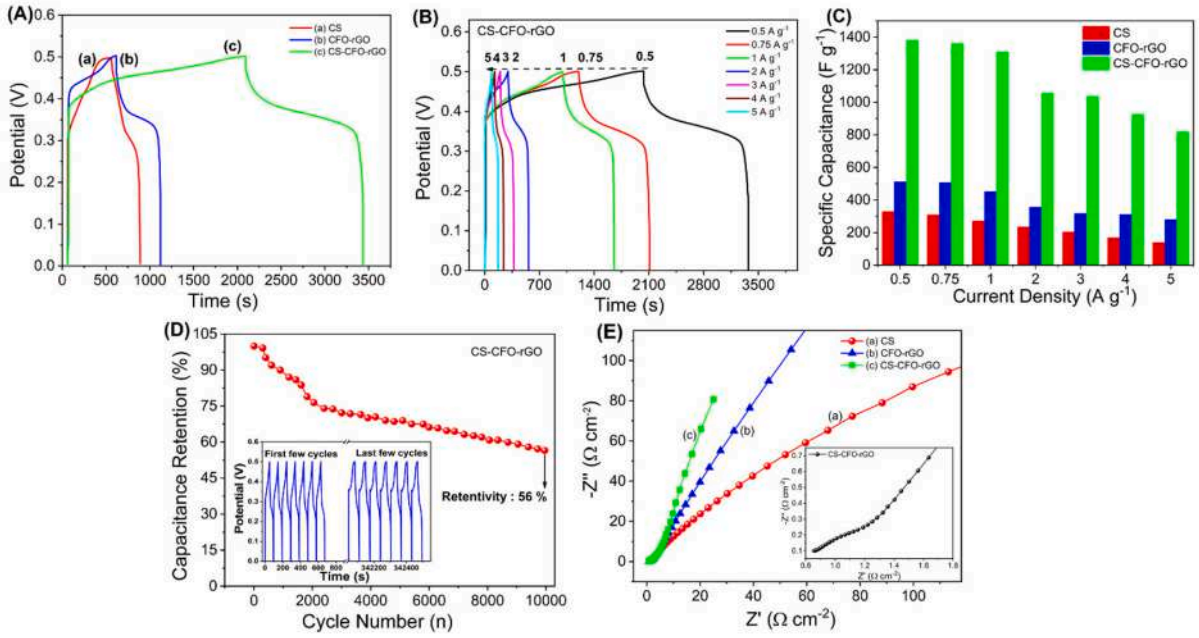


**Fig. 7.** (A) GCD curves of CS (a), CFO-rGO (b), and CS-CFO-rGO (c) at 0.5 A $g^{-1}$. (B) GCD curves of CS-CFO-rGO at 0.5, 0.75, 1, 2, 3, 4, and 5 A $g^{-1}$ current densities. (C) A plot of the relationship between specific capacitance of CS, CFO-rGO, and CS-CFO-rGO and current densities. (D) GCD cyclic stability of CS-CFO-rGO electrode at 10 A $g^{-1}$ current density with inset showing initial and final few GCD cycles. (E) Nyquist plots of CS, CFO-rGO, and CS-CFO-rGO. The lower inset displays the enlarged view of the Nyquist plot of CS-CFO-rGO and the upper inset shows the equivalent Randles circuit to fit the experimental data.

EIS was utilized to evaluate the interfacial and charge transfer behaviors of CS, CFO-rGO, and CS-CFO-rGO. The impedance was measured at 30 KHz to 0.01 Hz employing an amplitude of 0.005 *V*/s. The Nyquist plots of the CS, CFO-rGO, and CS-CFO-rGO samples are shown in Fig. 7E along with the enlarged view of the Nyquist plot of CS-CGO-rGO in the lower inset. An incomplete semi-circle observed in the Nyquist plots at the high-frequency zone is indicative of a capacitive behaviour due to the unequal current distribution on the electrode surface [72]. Furthermore, a 45° slope diagonal line on a Nyquist plot represents Warburg impedance resulting from a diffusion process. The EIS data were analyzed by electrical circuit models and depicted in the S.I. (Fig. S9). The resulting experimental and circuit-fitted values of bulk electrolyte resistance ($R_s$) and charge transfer resistance ($R_{ct}$) of CS, CFO-rGO, and CS-CFO-rGO are summarized in Table S2. The CS-CFO-rGO has a lower $R_s$ (0.829 Ω) and $R_{ct}$ (1.10 Ω) compared to the CS and CFO-rGO. The lower values of $R_s$ and $R_{ct}$ for CS-CFO-rGO are attributed to the combined effect of

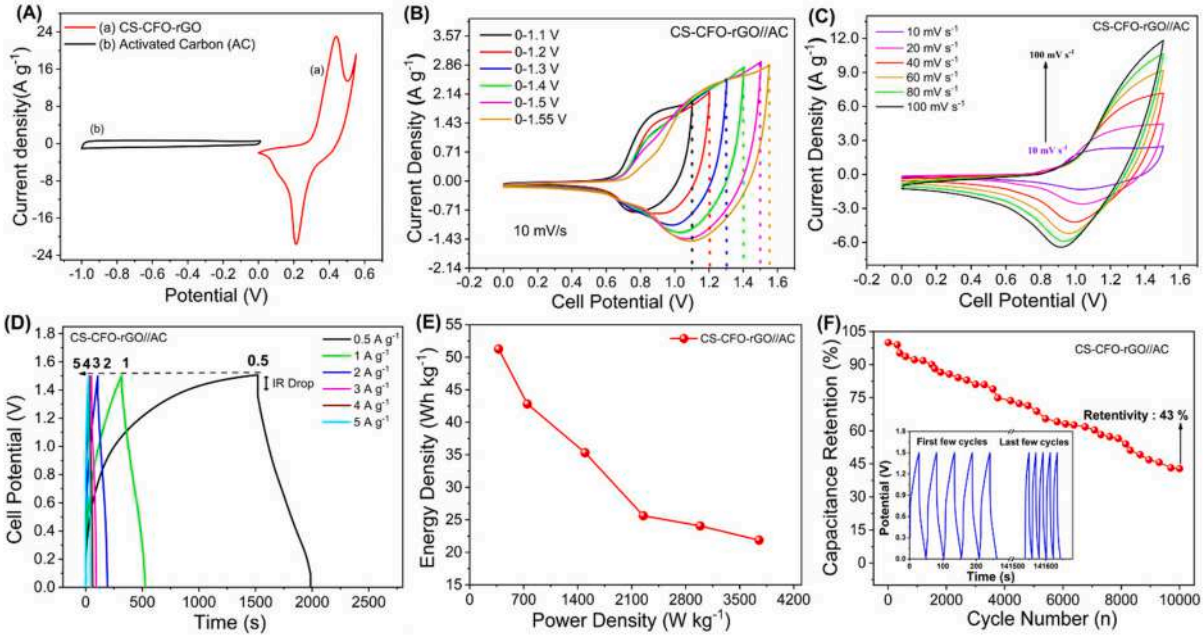


**Fig. 8.** (A) CV curves of Activated carbon (AC) and CS-CFO-rGO at a scan rate of 10 mV $s^{-1}$. (B) CV curves of the CS-CFO-rGO//AC asymmetric device at various potential windows. (C) CV curves of the CS-CFO-rGO//AC asymmetric device at 10 to 100 mV $s^{-1}$ scan rate. (D) GCD performance of the CS-CFO-rGO//AC asymmetric device at various current densities. (E) A Ragone plot of CS-CFO-rGO//AC asymmetric device. (F) GCD cyclic stability of CS-CFO-rGO//AC asymmetric device at 5 A $g^{-1}$ current density with inset showing first and last few GCD cycles.

interconnected nanoflake-like porous structure that shortens the path of ion transfer and higher conductivity of rGO.

### 3.3. Electrochemical performance of asymmetric supercapacitors

To demonstrate the applicability of CS-CFO-rGO, an ASC device was constructed using all solid-state designs. The ASC device was built by using CS-CFO-rGO positive electrode and activated carbon negative electrode, and it is designated as CS-CFO-rGO//AC. For the measurements of the ASC device with a two-electrode system, it is necessary to optimize the potential window and the mass ratio of the two electrodes of the ASC device. This can be done by using eq. 10, which calculates the mass balance, by considering the specific capacitance ($C_{sp}$), the mass of each electrode (m), and the potential difference ($\Delta V$) for the anode (+) and cathode (−) [73].

$$\frac{m^+}{m^-} = \frac{C_{SP^-}\Delta V^-}{C_{SP^+}\Delta V^+} \tag{10}$$

The optimum mass proportion has been determined to be 0.13 to ensure a balanced charge capacity on each electrode of the CS-CFO-rGO//AC asymmetric cell. Fig. 8A displays the comparative CV curves obtained from both activated carbon and CS-CFO-rGO electrodes, recorded utilizing a 3-electrode system, with a scan rate of 10 mV $s^{-1}$. The CV curve of the activated carbon was found to have a rectangular appearance within the potential window of −1 to 0 V. On the other hand, the CV profile of CS-CF-rGO exhibited redox activity in a potential window of 0 to 0.55 V. To determine the potential window for the CS-CFO-rGO//AC ASC device, a series of CVs were conducted. These CVs were measured using a scan rate of 10 mV $s^{-1}$ and the potential window gradually extended from 0.0 to 1.0 V up to 0.0 to 1.55 V, as depicted in Fig. 8B. An asymmetric supercapacitor exhibits stable capacitive behaviour in 0 to 1.5 V, without experiencing oxygen evolution or polarization effects. As a result, for further examination, a potential window of 0 to 1.5 V was chosen. By expanding the operating potential window, the E.D. of asymmetric supercapacitors can be significantly increased. The CV profiles of the device at various scan rates (10–100 mV $s^{-1}$) within the potential window of 0 to 1.5 V are shown in Fig. 8C. For a more detailed view at slower scan rates (1–10 mV $s^{-1}$), refer to Fig. S10. As the scan rate increased, the enclosed area of the CV curves grew proportionally, without altering their fundamental shape. This consistent profile indicates the device's efficient performance even under high scan rates. Fig. 8D illustrates the GCD curves of the CS-CFO-rGO//AC supercapacitor across various current densities ranging from 0.5 to 5 A $g^{-1}$. The GCD curves display a well-balanced charge and discharge behaviour with minimal polarization even at low current densities. The specific capacitances (Cs) of the CS-CFO-rGO//AC device calculated using eq. 9 were 164, 137, 113, 82, 77, and 70 F $g^{-1}$ at corresponding current densities of 0.5, 1, 2, 3, 4, and 5 A $g^{-1}$, respectively.

The evaluation of supercapacitor performance is greatly influenced by two key metrics: E.D. and P.D. and are computed using equations given below,

$$\text{E.D.}\left(\text{Wh kg}^{-1}\right) = 0.5\ \frac{C_{SP}\ (V_{2-}V_1)^2}{3.6} \tag{11}$$

$$\text{P.D.}\left(\text{W kg}^{-1}\right) = \frac{\text{E.D.}}{\Delta t}3600 \tag{12}$$

Where '$(V_2 - V_1)^{2}$' is the potential window, and '$\Delta t$' is the discharge time. The Ragone plot of the CS-CFO-rGO//AC ASC device determined using eqs. (11) and (12) is shown in Fig. 8E. The ASC device delivered E.D. of 55.25, 42.81, 35.31, 25.62, 24.06, and 21.87 Wh $kg^{-1}$ at P.D. of 375, 748.13, 1495.5, 2250, 2987, and 3750 W $kg^{-1}$, respectively. A Ragone plot, comparing the energy and power densities of the CS-CFO-rGO//AC ASC device with reported literature is given in Fig. S11.

The electrochemical cyclic stability of the CS-CFO-rGO//AC ASC device is tested by conducting 10,000 GCD cycles at 5 A $g^{-1}$ after activating the material for 1500 cycles with an inset showing the GCD curves at the beginning and end of 10,000 cycles (Fig. 8F). Cycling the electrode initially can improve its performance by promoting more complete intercalation and de-intercalation of ions and gives stable cyclic performance [74]. After 2000 GCD cycles, 85 % capacitance was retained for the CS-CFO-rGO//AC ASC device which decreased to 43 % after 10,000 cycles. The improved cyclic performance of the CS-CFO-rGO//AC ASC device is possibly due to both the chemical and mechanical stability of the electrode materials and the polymer gel electrolyte. The Nyquist and Bode plots of the CS-CFO-rGO//AC ASC device after 10,000 GCD cycles are shown in Fig. S12. The Nyquist plot reveals $R_{ct}$ of 6.5 Ω and $R_s$ of 2.3 Ω. The relaxation time ($\tau_0 = f_0^{-1}$) determined from the knee frequency, represents the shortest time required for the device to effectively dissipate all its stored energy, exceeding a 50 % efficiency threshold [75]. The calculated relaxation time constant ($\tau_0$) is 169 ms for the CS-CFO-rGO//AC ASC device after 10,000 GCD cycles.

Finally, we demonstrated the potential usefulness of the assembled CS-CFO-rGO//AC ASC device by powering light-emitting diodes (LEDs). For this, two CS-CFO-rGO//AC asymmetric devices were linked in a series and charged using a 3 *V* DC battery for 60 s. Then red or green LEDs were connected to the charged capacitors. The fabricated CS-CFO-rGO//AC device successfully lit up the red and green LEDs for 68 s and 30 s, respectively (Fig. 9) and videos are provided as supporting video 1 and supporting video 2 in supporting information.

## 4. Conclusions

In summary, CS, CFO-rGO, and CS-CFO-rGO nanohybrids were successfully synthesized using a hydrothermal approach to develop a high-energy density supercapacitor. In CS-CFO-rGO hybrid nanocomposite, the flower-like architecture of CS composed of many crossed nanoplates with abundant ordered pores provides a large specific surface area. Conductive rGO provides anchoring sites for the deposition of CS and CFO nanoparticles and reduces electrical resistance. XPS investigations and ab initio DFT calculations indicate the presence of cobalt ferrite nanocrystals with both normal and inverse occupation types, which is the most suitable phase of CFO for supercapacitor applications. Furthermore, CS and CFO both offer rich redox chemistry for electrolyte accessibility and faradaic processes and also avoid restacking of rGO. The ternary composite showcased remarkable enhancement in specific capacitance, reaching 1381 F $g^{-1}$ compared to that of CS (329 F $g^{-1}$) and CFO-rGO (511 F $g^{-1}$) at 0.5 A $g^{-1}$. The enhancement in the overall supercapacitive performance of the CS-CFO-rGO composite is probably due to the combined benefits of the pseudo and double-layer capacitive contributions of its various components. The practical application of the CS- CFO-rGO ternary nanohybrid was also demonstrated by fabricating an all-solid-state asymmetric supercapacitor CS- CFO-rGO//AC. The ASC device delivered 164 F $g^{-1}$ capacitance with 55.25 Wh $kg^{-1}$ energy density and 375 W $Kg^{-1}$ power density at a stable output potential of 1.5 V. Moreover, the assembled device retained 43 % of its original capacitance following 10,000 charge-discharge cycles, showing satisfactory cycling stability. The fabricated ASC device could glow red and green LEDs. This work emphasizes the potential of CS- CFO-rGO ternary nanohybrid as high-energy electrode material for all-solid-state asymmetric SCs.

Supplementary data to this article can be found online at https://doi.org/10.1016/j.est.2024.114842.

## CRediT authorship contribution statement

**S.R. Shingte:** Writing – original draft, Methodology, Formal analysis, Data curation. **A.M. Patil:** Writing – review & editing, Data curation. **Sibylle Gemming:** Visualization, Software, Formal analysis, Data curation. **D.R.T. Zahn:** Visualization, Formal analysis. **T.D. Dongale:**

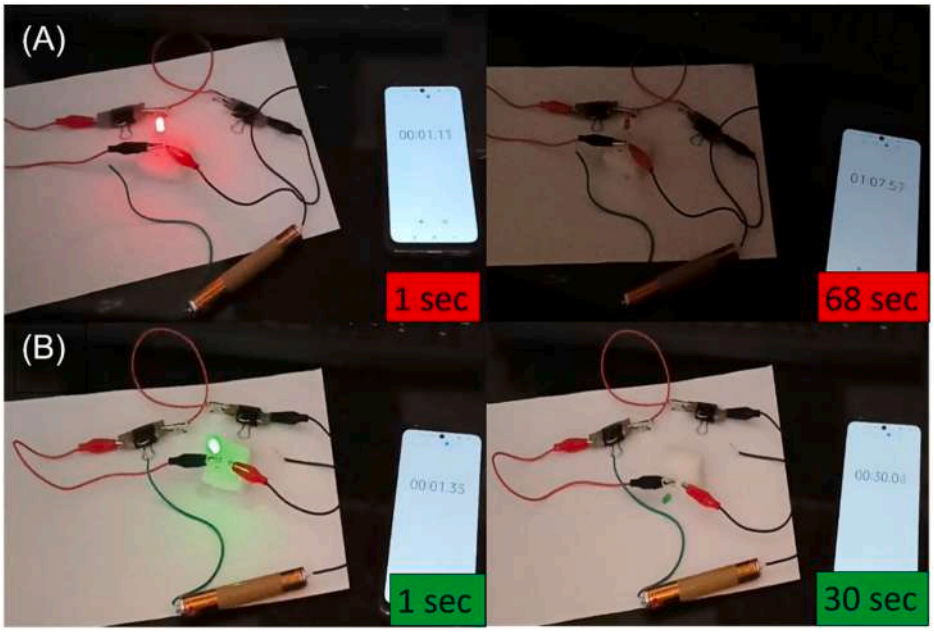


**Fig. 9.** Digital photographs of the CS-CFO-rGO//AC asymmetric device glowing red (A) and green LED (B). (For interpretation of the references to colour in this figure legend, the reader is referred to the web version of this article.)

Visualization, Formal analysis. **Seong Chan Jun:** Writing – review & editing, Visualization, Supervision. **G. Salvan:** Writing – review & editing, Visualization, Formal analysis. **P.B. Patil:** Writing – review & editing, Supervision, Project administration, Investigation, Conceptualization.

## Declaration of competing interest

The authors declare that they have no known competing financial interests or personal relationships that could have appeared to influence the work reported in this paper.

## Acknowledgments

PB Patil acknowledges the visiting scholarship provided by Chemnitz University of Technology, Germany. SR Shingte is thankful to the Chhatrapati Shahu Maharaj Research, Training, and Human Development Institute (SARTHI) for the fellowship. This work is supported by the Science and Engineering Research Board, Department of Science and Technology (DST-SERB), Government of India (no. EMR/2017/001810), Deutsche Forschungsgemeinschaft (DFG) (405595647, 449119662, 514664767), and the Brain Pool Program through the National Research Foundation of Korea (NRF), funded by the Ministry of Science and Information and Communication Technologies (ICT) (2020H1D3A1A04105926).

## Data availability

The data that has been used is confidential.

## References

[1] A.G. Olabi, Q. Abbas, A. Al Makky, M.A. Abdelkareem, Supercapacitors as next generation energy storage devices: properties and applications, Energy 248 (2022), https://doi.org/10.1016/j.energy.2022.123617.
[2] Q. Abbas, S.H. Siyal, A. Mateen, M.A. Bajaber, A. Ahmad, M.S. Javed, P. Martin, N. Joly, P. Bocchetta, Flower-like highly open-structured binder-free Zn-co-oxide Nanosheet for high-performance supercapacitor electrodes, Molecules 27 (2022) 4880, https://doi.org/10.3390/molecules27154850.
[3] L. Yue, S. Zhang, H. Zhao, Y. Feng, M. Wang, L. An, X. Zhang, J. Mi, One-pot synthesis $CoFe_2O_4$/CNTs composite for asymmetric supercapacitor electrode, Solid State Ionics 329 (2019) 15–24, https://doi.org/10.1016/j.ssi.2018.11.006.
[4] N.I. Jalal, R.I. Ibrahim, M.K. Oudah, A review on supercapacitors: types and components, J. Phys. Conf. Ser. 1973 (2021), https://doi.org/10.1088/1742-6596/1973/1/012015.
[5] R.S. Desai, V.S. Jadhav, P.S. Patil, D.S. Dalavi, Recent advances in hydrothermally and solvothermally grown $Co_3O_4$ nanostructures for electrochemical energy storage (EES) applications: a brief review, Mater. Adv. 5 (2024) 920–960, https://doi.org/10.1039/d3ma00806a.
[6] K. Mensah-Darkwa, D.N. Ampong, E. Agyekum, F.M. de Souza, R.K. Gupta, Recent advancements in chalcogenides for electrochemical energy storage applications, Energies 15 (2022) 1–62, https://doi.org/10.3390/en15114052.
[7] Y. An, C., Zhang, Y., Guo, H., & Wang, Metal oxide-based supercapacitors_ progress and prospectives, Nanoscale. (2019) 4644–4658. doi:https://doi.org/10.1039/c9na00543a.
[8] J. Hanzig, M. Zschornak, M. Nentwich, F. Hanzig, S. Gemming, T. Leisegang, D. C. Meyer, Strontium titanate: An all-in-one rechargeable energy storage material, J. Power Sources 267 (2014) 700–705, https://doi.org/10.1016/j.jpowsour.2014.05.095.
[9] M. Manuraj, K.V. Kavya Nair, K.N.N. Unni, R.B. Rakhi, High performance supercapacitors based on $MoS_2$ nanostructures with near commercial mass loading, J. Alloys Compd. 819 (2020) 152963, https://doi.org/10.1016/j.jallcom.2019.152963.
[10] W. Dong, X. Wang, B. Li, L. Wang, B. Chen, C. Li, X. Li, T. Zhang, Z. Shi, Hydrothermal synthesis and structure evolution of hierarchical cobalt sulfide nanostructures, Dalton Trans. 40 (2011) 243–248, https://doi.org/10.1039/c0dt01107j.
[11] Q. Hu, S. Zhang, W. Li, J. Xiong, X. Zou, H. Shen, Regulating the structure and morphology of nickel sulfides for electrochemical energy storage: the role of solvent pH, Chem. Eng. J. 441 (2022) 136130, https://doi.org/10.1016/j.cej.2022.136130.
[12] R.B. Pujari, A.C. Lokhande, A.A. Yadav, J.H. Kim, C.D. Lokhande, Synthesis of MnS microfibers for high performance flexible supercapacitors, Mater. Des. 108 (2016) 510–517, https://doi.org/10.1016/j.matdes.2016.07.038.
[13] S.S. Karade, P. Dwivedi, S. Majumder, B. Pandit, B.R. Sankapal, First report on a FeS-based 2 V operating flexible solid-state symmetric supercapacitor device, sustain, Energy Fuel 1 (2017) 1366–1375, https://doi.org/10.1039/C7SE00165G.
[14] L. Xu, Y. Lu, One-step synthesis of a cobalt sulfide/reduced graphene oxide composite used as an electrode material for supercapacitors, RSC Adv. 5 (2015) 67518–67523, https://doi.org/10.1039/c5ra11711a.
[15] B. Guan, S.Y. Qi, Y. Li, T. Sun, Y.G. Liu, T.F. Yi, Towards high-performance anodes: design and construction of cobalt-based sulfide materials for sodium-ion batteries, J. Energy Chem. 54 (2021) 680–698, https://doi.org/10.1016/j.jechem.2020.06.005.
[16] S.M. Nikam, A. Sharma, M. Rahaman, A.M. Teli, S.H. Mujawar, D.R.T. Zahn, P. S. Patil, S.C. Sahoo, G. Salvan, P.B. Patil, Pulsed laser deposited $CoFe_2O_4$ thin films as supercapacitor electrodes, RSC Adv. 10 (2020) 19353–19359, https://doi.org/10.1039/d0ra02564j.

[17] D.M. El-Gendy, I.M. Afifi, N.K. Allam, Eco-friendly, one-step synthesis of cobalt sulfide-decorated functionalized graphene for high-performance supercapacitors, J. Energy Storage. 24 (2019), https://doi.org/10.1016/j.est.2019.100760.

[18] P. Liu, H. Chen, X. Chang, Y. Xue, J. Zhou, Z. Zhao, H. Lin, S. Han, Novel method of preparing $CoFe_2O_4$/graphene by using steel rolling sludge for supercapacitor, Electrochim. Acta 231 (2017) 565–574, https://doi.org/10.1016/j.electacta.2017.02.088.

[19] J. Yuan, L. Jiang, J. Che, G. He, H. Chen, Composites of $NiS_2$ microblocks, $MoS_2$ Nanosheets, and reduced graphene oxide for energy storage and electrochemical detection of bisphenol a, ACS Appl. Nano Mater. 4 (2021) 6093–6102, https://doi.org/10.1021/acsanm.1c00908.

[20] T. Liu, J. Liu, L. Zhang, B. Cheng, J. Yu, Construction of nickel cobalt sulfide nanosheet arrays on carbon cloth for performance-enhanced supercapacitor, J. Mater. Sci. Technol. 47 (2020) 113–121, https://doi.org/10.1016/j.jmst.2019.12.027.

[21] H. Shangguan, W. Huang, C. Engelbrekt, X. Zheng, F. Shen, X. Xiao, L. Ci, P. Si, J. Zhang, Well-defined cobalt sulfide nanoparticles locked in 3D hollow nitrogen-doped carbon shells for superior lithium and sodium storage, Energy Storage Mater. 18 (2019) 114–124, https://doi.org/10.1016/j.ensm.2019.01.012.

[22] K. Vijaya Sankar, R. Kalai Selvan, Fabrication of flexible fiber supercapacitor using covalently grafted $CoFe_2O_4$/reduced graphene oxide/polyaniline and its electrochemical performances, Electrochim. Acta 213 (2016) 469–481, https://doi.org/10.1016/j.electacta.2016.07.056.

[23] Y. Zhao, L. Xu, J. Yan, W. Yan, C. Wu, J. Lian, Y. Huang, J. Bao, J. Qiu, L. Xu, Y. Xu, H. Xu, H. Li, Facile preparation of $NiFe_2O_4/MoS_2$ composite material with synergistic effect for high performance supercapacitor, J. Alloys Compd. 726 (2017) 608–617, https://doi.org/10.1016/j.jallcom.2017.07.327.

[24] S. Sharifi, K. Rahimi, A. Yazdani, Highly improved supercapacitance properties of $MnFe_2O_4$ nanoparticles by $MoS_2$ nanosheets, Sci. Rep. 11 (2021) 1–15, https://doi.org/10.1038/s41598-021-87823-6.

[25] P. Salarizadeh, M.B. Askari, K. Hooshyari, H. Saeidfirozeh, Synergistic effect of $MoS_2$ and $Fe_3O_4$ decorated reduced graphene oxide as a ternary hybrid for high-performance and stable asymmetric supercapacitors, Nanotechnology 31 (2020), https://doi.org/10.1088/1361-6528/aba1bd.

[26] M.M. Ovhal, N. Kumar, S.K. Hong, H.W. Lee, J.W. Kang, Asymmetric supercapacitor featuring carbon nanotubes and nickel hydroxide grown on carbon fabric: a study of self-discharging characteristics, J. Alloys Compd. 828 (2020) 154447, https://doi.org/10.1016/j.jallcom.2020.154447.

[27] S. Sharma, P. Chand, Ultrahigh energy and power density of zeolitic imidazolate framework-8 asymmetric and symmetric supercapacitors in an organic electrolyte for energy storage devices, J. Energy Storage. 94 (2024), https://doi.org/10.1016/j.est.2024.112459.

[28] S. Kaushik, P. Chand, S. Sharma, Asymmetric supercapacitor device fabrication of pristine Zeolitic Imidazolate Framework-67 with ultrahigh performance and cyclic stability, J. Energy Storage. 78 (2024), https://doi.org/10.1016/j.est.2023.110033.

[29] H. Gao, J. Xiang, Y. Cao, Hierarchically porous $CoFe_2O_4$ nanosheets supported on Ni foam with excellent electrochemical properties for asymmetric supercapacitors, Appl. Surf. Sci. 413 (2017) 351–359, https://doi.org/10.1016/j.apsusc.2017.04.067.

[30] X. Li, Q. Li, Y. Wu, M. Rui, H. Zeng, Two-Dimensional , Porous Nickel-Cobalt Sulfide for High-Performance Asymmetric Supercapacitors Nickel-Cobalt Sulfide Nanosheets with Ultrathin Thickness and Abundant Pores for High-Performance Asymmetric Supercapacitors, Appl. Mater. Interfaces 7 (2015) 19316–19323. doi: https://doi.org/10.1021/acsami.5b05400.

[31] S. Sharma, P. Chand, Zeolitic Imidazolate Framework-8 and redox-additive electrolyte based asymmetric supercapacitor: a synergetic combination for ultrahigh energy and power density, J. Energy Storage. 73 (2023), https://doi.org/10.1016/j.est.2023.108961.

[32] K. Ashok Kumar, A. Pandurangan, S. Arumugam, M. Sathiskumar, Effect of bi-functional hierarchical flower-like CoS nanostructure on its interfacial charge transport kinetics, magnetic and electrochemical behaviors for supercapacitor and DSSC applications, Sci. Rep. 9 (2019) 1–16, https://doi.org/10.1038/s41598-018-37463-0.

[33] R.K. Singh, R. Kumar, D.P. Singh, Graphene oxide: strategies for synthesis, reduction and frontier applications, RSC Adv. 6 (2016) 64993–65011, https://doi.org/10.1039/c6ra07626b.

[34] H. Vijeth, S.P. Ashokkumar, L. Yesappa, M. Niranjana, M. Vandana, H. Devendrappa, Flexible and high energy density solid-state asymmetric supercapacitor based on polythiophene nanocomposites and charcoal, RSC Adv. 8 (2018) 31414–31426, https://doi.org/10.1039/c8ra06102e.

[35] Q. Liu, J. Zhang, A general and controllable synthesis of $Co_mS_n$ ($Co_9S_8$, $Co_3S_4$, and $Co_{1-x}S$) hierarchical microspheres with homogeneous phases, CrystEngComm 15 (2013) 5087–5092, https://doi.org/10.1039/c3ce40251g.

[36] P. He, K. Yang, W. Wang, F. Dong, L. Du, Y. Deng, Reduced graphene oxide-$CoFe_2O_4$ composites for supercapacitor electrode, Russ. J. Electrochem. 49 (2013) 359–364, https://doi.org/10.1134/S1023193513040101.

[37] J. Prasad, A.K. Singh, M. Tomar, V. Gupta, K. Singh, High-efficiency microwave absorption and electromagnetic interference shielding of cobalt-doped $MoS_2$ nanosheet anchored on the surface reduced graphene oxide nanosheet, J. Mater. Sci. Mater. Electron. 31 (2020) 19895–19909, https://doi.org/10.1007/s10854-020-04512-2.

[38] A. Monshi, M.R. Foroughi, M.R. Monshi, Modified Scherrer equation to estimate more accurately Nano-crystallite size using XRD, World J. Nano Sci. Eng. 02 (2012) 154–160, https://doi.org/10.4236/wjnse.2012.23020.

[39] G. Surender, F.S. Omar, S. Bashir, M. Pershaanaa, S. Ramesh, K. Ramesh, Growth of nanostructured cobalt sulfide-based nanocomposite as faradaic binder-free electrode for supercapattery, J. Energy Storage. 39 (2021) 102599, https://doi.org/10.1016/j.est.2021.102599.

[40] T. Xu, Z. Wang, G. Wang, L. Lu, S. Liu, S. Gao, H. Xu, Z. Yu, One-pot synthesis of a CoS-AC electrode in a redox electrolyte for high-performance supercapacitors, J. Appl. Electrochem. 49 (2019) 1069–1077, https://doi.org/10.1007/s10800-019-01341-y.

[41] J. Mujtaba, L. He, H. Zhu, Z. Xiao, G. Huang, A.A. Solovev, Y. Mei, $Co_9S_8$ nanoparticles for hydrogen evolution, ACS Appl. Nano Mater. 4 (2021) 1776–1785, https://doi.org/10.1021/acsanm.0c03171.

[42] S.M. Ansari, K.C. Ghosh, R.S. Devan, D. Sen, P.U. Sastry, Y.D. Kolekar, C. V. Ramana, Eco-friendly synthesis, crystal chemistry, and magnetic properties of manganese-substituted $CoFe_2O_4$ nanoparticles, ACS Omega 5 (2020) 19315–19330, https://doi.org/10.1021/acsomega.9b02492.

[43] K.V. Sankar, R.K. Selvan, D. Meyrick, Electrochemical performances of $CoFe_2O_4$ nanoparticles and a rGO based asymmetric supercapacitor, RSC Adv. 5 (2015) 99959–99967, https://doi.org/10.1039/c5ra14938j.

[44] L. Zheng, L. Guan, G. Yang, S. Chen, H. Zheng, One-pot synthesis of $CoFe_2O_4$/rGO hybrid hydrogels with 3D networks for high capacity electrochemical energy storage devices, RSC Adv. 8 (2018) 8607–8614, https://doi.org/10.1039/c8ra00285a.

[45] A. De Adhikari, R. Oraon, S.K. Tiwari, P. Saren, J.H. Lee, N.H. Kim, G.C. Nayak, CdS-$CoFe_2O_4$@reduced graphene oxide Nanohybrid: An excellent electrode material for supercapacitor applications, Ind. Eng. Chem. Res. 57 (2018) 1350–1360, https://doi.org/10.1021/acs.iecr.7b04885.

[46] L.T. Thanh Tam, D.T. Tung, H.M. Nguyet, N.T. Ngoc Linh, N.T. Dung, N. Van Quynh, N. Van Dang, D. Vernardou, T.K. Le, L.A. Tuan, P.N. Minh, L.T. Lu, High electrochemical performance of ink solution based on manganese cobalt sulfide/reduced graphene oxide nano-composites for supercapacitor electrode materials, RSC Adv. 12 (2022) 20182–20190, https://doi.org/10.1039/d2ra02818b.

[47] V. Mahdikhah, S. Saadatkia, S. Sheibani, A. Ataie, Outstanding photocatalytic activity of $CoFe_2O_4$/rGO nanocomposite in degradation of organic dyes, Opt. Mater. (Amst). 108 (2020) 110193, https://doi.org/10.1016/j.optmat.2020.110193.

[48] C. Zhao, X. Shao, Y. Zhang, X. Qian, Fe2O3/reduced graphene oxide/$Fe_3O_4$ composite in situ grown on Fe foil for high-performance supercapacitors 8 (2016) 30133–30142.

[49] J. Tan, Z. Wang, G. Li, H. Hu, J. Li, R. Han, D. Zhang, Electrochemically driven phase transition in $LiCoO_2$ cathode, Materials (Basel). 14 (2021) 1–10, https://doi.org/10.3390/ma14020242.

[50] C. Teng, F. Yang, M. Sun, K. Yin, Q. Huang, G. Fu, C. Zhang, X. Lu, J. Jiang, Structural and defect engineering of cobaltosic oxide nanoarchitectures as an ultrahigh energy density and super durable cathode for Zn-based batteries, Chem. Sci. 10 (2019) 7600–7609, https://doi.org/10.1039/c9sc01902b.

[51] R.S. Yadav, I. Kuřitka, J. Vilcakova, J. Havlica, J. Masilko, L. Kalina, J. Tkacz, J. Švec, V. Enev, M. Hajdúchová, Impact of grain size and structural changes on magnetic, dielectric, electrical, impedance and modulus spectroscopic characteristics of $CoFe_2O_4$ nanoparticles synthesized by honey mediated sol-gel combustion method, Adv. Nat. Sci. Nanosci. Nanotechnol. 8 (2017), https://doi.org/10.1088/2043-6254/aa853a.

[52] K.J. Huang, J.Z. Zhang, G.W. Shi, Y.M. Liu, One-step hydrothermal synthesis of two-dimensional cobalt sulfide for high-performance supercapacitors, Mater. Lett. 131 (2014) 45–48, https://doi.org/10.1016/j.matlet.2014.05.148.

[53] K. Krishnamoorthy, G.K. Veerasubramani, S.J. Kim, Hydrothermal synthesis, characterization and electrochemical properties of cobalt sulfide nanoparticles, Mater. Sci. Semicond. Process. 40 (2015) 781–786, https://doi.org/10.1016/j.mssp.2015.06.070.

[54] S. Martinez-Vargas, A.I. Mtz-Enriquez, H. Flores-Zuñiga, A. Encinas, J. Oliva, Enhancing the capacitance and tailoring the discharge times of flexible graphene supercapacitors with cobalt ferrite nanoparticles, Synth. Met. 264 (2020) 116384, https://doi.org/10.1016/j.synthmet.2020.116384.

[55] P.J. Sephra, P. Baraneedharan, M. Sivakumar, T.D. Thangadurai, K. Nehru, In situ growth of hexagonal-shaped α-$Fe_2O_3$ nanostructures over few layered graphene by hydrothermal method and their electrochemical performance, J. Mater. Sci. Mater. Electron. 29 (2018) 6898–6908, https://doi.org/10.1007/s10854-018-8676-1.

[56] W. Yan, X. Cao, K. Ke, J. Tian, C. Jin, R. Yang, One-pot synthesis of monodispersed porous $CoFe_2O_4$ nanospheres on graphene as an efficient electrocatalyst for oxygen reduction and evolution reactions, RSC Adv. 6 (2015) 307–313, https://doi.org/10.1039/c5ra23306b.

[57] K.S. Sing, Reporting physisorption data for gas/solid systems with special reference to the determination of surface area and porosity, pure app!, Chem 57 (1985) 603–619, https://doi.org/10.1351/pac198557040603.

[58] L. Gao, E. Han, Y. He, C. Du, J. Liu, X. Yang, Effect of different templating agents on cobalt ferrite ($CoFe_2O_4$) nanomaterials for high-performance supercapacitor, Ionics (Kiel). 26 (2020) 3643–3654, https://doi.org/10.1007/s11581-020-03482-z.

[59] V.S. Bhat, S. S, T.J. Jayeoye, T. Rujiralai, U. Sirimahachai, K.F. Chong, G. Hegde, Influence of surface properties on electro-chemical supercapacitors utilizing Callerya atropurpurea pod derived porous nanocarbons: structure property relationship between porous structures to energy storage devices, Nano Sel. 1 (2020) 226–243, https://doi.org/10.1002/nano.202000013.

[60] S. Ranganatha, Mesoporous materials for high- performance electrochemical supercapacitors, Mesoporous Mater. Appl. (2019), https://doi.org/10.1021/bk-2020-1353.ch004.

[61] S. Peng, L. Li, Y. Hu, M. Srinivasan, F. Cheng, J. Chen, S. Ramakrishna, Fabrication of spinel one-dimensional architectures by single-spinneret electrospinning for

energy storage applications, ACS Nano 9 (2015) 1945–1954, https://doi.org/10.1021/nn506851x.
[62] H. Li, Z. Li, Z. Wu, M. Sun, S. Han, C. Cai, W. Shen, Y. Fu, Nanocomposites of cobalt sulfide embedded carbon nanotubes with enhanced supercapacitor performance, J. Electrochem. Soc. 166 (2019) A1031–A1037, https://doi.org/10.1149/2.0531906jes.
[63] S. Sahoo, C.S. Rout, Facile electrochemical synthesis of porous manganese-cobalt-sulfide based ternary transition metal sulfide Nanosheets architectures for high performance energy storage applications, Electrochim. Acta 220 (2016) 57–66, https://doi.org/10.1016/j.electacta.2016.10.043.
[64] S.J. Bao, C.M. Li, C.X. Guo, Y. Qiao, Biomolecule-assisted synthesis of cobalt sulfide nanowires for application in supercapacitors, J. Power Sources 180 (2008) 676–681, https://doi.org/10.1016/j.jpowsour.2008.01.085.
[65] J. Luo, J. Wang, S. Liu, W. Wu, T. Jia, Z. Yang, S. Mu, Y. Huang, Graphene quantum dots encapsulated tremella-like $NiCo_2O_4$ for advanced asymmetric supercapacitors, Carbon N. Y. 146 (2019) 1–8, https://doi.org/10.1016/j.carbon.2019.01.078.
[66] B. Rani, N.K. Sahu, Electrochemical properties of $CoFe_2O_4$ nanoparticles and its rGO composite for supercapacitor, Diam. Relat. Mater. 108 (2020) 107978, https://doi.org/10.1016/j.diamond.2020.107978.
[67] N. Elgrishi, K.J. Rountree, B.D. McCarthy, E.S. Rountree, T.T. Eisenhart, J. L. Dempsey, A practical Beginner's guide to cyclic voltammetry, J. Chem. Educ. 95 (2018) 197–206, https://doi.org/10.1021/acs.jchemed.7b00361.
[68] K.J. Aoki, J. Chen, Y. Liu, B. Jia, Peak potential shift of fast cyclic voltammograms owing to capacitance of redox reactions, J. Electroanal. Chem. 856 (2020) 113609, https://doi.org/10.1016/j.jelechem.2019.113609.
[69] P.D. Patil, S.R. Shingte, V.C. Karade, J.H. Kim, T.D. Dongale, S.H. Mujawar, A. M. Patil, P.B. Patil, Effect of annealing temperature on morphologies of metal organic framework derived $NiFe_2O_4$ for supercapacitor application, J. Energy Storage. 40 (2021) 102821, https://doi.org/10.1016/j.est.2021.102821.
[70] J. Liu, J. Wang, C. Xu, H. Jiang, C. Li, L. Zhang, J. Lin, Z.X. Shen, Advanced energy storage devices: basic principles, analytical methods, and rational materials design, Adv. Sci. 5 (2018), https://doi.org/10.1002/advs.201700322.
[71] T. Liu, How to Differentiate Capacitances Using Trasatti and Dunn Methods, 2018.
[72] Q. Cheng, Z. Chen, The cause analysis of the incomplete semi-circle observed in high frequency region of EIS obtained from TEL-covered pure copper, Int. J. Electrochem. Sci. 8 (2013) 8282–8290.
[73] M.R. Thalji, G.A.M. Ali, P. Liu, Y.L. Zhong, K.F. Chong, $W_{18}O_{49}$ nanowires-graphene nanocomposite for asymmetric supercapacitors employing $AlCl_3$ aqueous electrolyte, Chem. Eng. J. 409 (2021) 128216, https://doi.org/10.1016/j.cej.2020.128216.
[74] X. Lu, D. Zheng, T. Zhai, Z. Liu, Y. Huang, S. Xie, Y. Tong, Facile synthesis of large-area manganese oxide nanorod arrays as a high-performance electrochemical supercapacitor, Energy Environ. Sci. 4 (2011) 2915–2921, https://doi.org/10.1039/c1ee01338f.
[75] S.R. Shingte, V.D. Chavan, R.P. Dhavale, D.K. Kim, H.H. Park, T.D. Dongale, P. B. Patil, Optimizing supercapacitive performance of MXene through MOF-derived nickel ferrite nanoparticle integration, J. Energy Storage. 92 (2024) 112169, https://doi.org/10.1016/j.est.2024.112169.